

Whistler wave generation by non-gyrotropic, relativistic, electron beams

M. Skender and D. Tsiklauri

*School of Physics and Astronomy, Queen Mary University of London,
327 Mile End Road, London, E1 4NS, United Kingdom*

Particle-in-cell code, EPOCH, is used for studying features of the wave component evident to propagate backwards from the front of the non-gyrotropic, relativistic beam of electrons injected in the Maxwellian, magnetised background plasma with decreasing density profile. According to recent findings presented in Tsiklauri (2011), Schmitz & Tsiklauri (2013) and Pechhacker & Tsiklauri (2012), in a 1.5-dimensional magnetised plasma system, the non-gyrotropic beam generates freely escaping electromagnetic radiation with properties similar to the Type-III solar radio bursts. In this study the backwards propagating wave component evident in the perpendicular components of the electromagnetic field in such a system is presented for the first time. Background magnetic field strength in the system is varied in order to prove that the backwards propagating wave's frequency, prescribed by the whistler wave dispersion relation, is proportional to the specified magnetic field. Moreover, the identified whistlers are shown to be generated by the normal Doppler-shifted relativistic resonance. Large fraction of the energy of the perpendicular electromagnetic field components is found to be carried away by the whistler waves, while a small but sufficient fraction is going into L- and R- electromagnetic modes.

I. INTRODUCTION

Narrow-band radio emissions originating from the Sun with well expressed impulsive onset at each frequency, known as the Type-III bursts, are characterised by well defined frequency drift and sometimes a separation of the emission pattern into two harmonics [4]. Super-thermal electron beams travelling away from the Sun on the open magnetic field lines are widely accepted to be the source of the Type-III bursts [5, 6]. The first and the most widely accepted mechanism for the generation of the Type-III bursts was based on the plasma emission. A fast moving ($0.2c - 0.5c$) electron beam excites Langmuir waves at the local plasma frequency, ω_p . The Langmuir waves are partially transformed via scattering at ω_p and $2\omega_p$, with ion sound and oppositely propagating Langmuir waves, respectively, into electromagnetic waves. As the electron beam propagates away from the Sun, through less dense coronal and interplanetary environment, the frequency of the emitted electromagnetic radiation decreases, because plasma frequency is a function of the square root of the plasma density.

Type-III bursts have been subject of theoretical, observational and numerical studies [7–10]. The first detailed theory of the Type-III emission invoked coherent plasma waves, generated by a stream of fast particles [11], which are due to Rayleigh and combination scattering at ω_p and $2\omega_p$ subsequently transformed into radio waves. Stochastic growth of the density irregularities was invoked in order to produce stochastically generated clumpy Langmuir waves, where the ambient density perturbations cause the beam to fluctuate around marginal stability [12]. Other mechanisms which generate the Type-III emission include: linear mode conversion of Langmuir waves [13], the antenna mechanism [14] and non-gyrotropic electron beam emission [1].

In Ref. [2] it was found that the non-gyrotropic beam excites electromagnetic radiation by (ω, k) -space drift

(or in other words wave refraction) while propagating along the 1-dimensional spatial domain throughout the decreasing plasma density profile. The analysis presented here reveals a new signal evident in the perpendicular components of the electromagnetic field in the scenario of the non-gyrotropic emission: A wave propagating backwards from the beam front. Investigation of the features of this wave component, its characterisation and its generation mechanism is topic of the presented numerical study. The background magnetic field was varied in order to prove the backwards travelling wave component's frequency to be proportional to the imposed background magnetic field. Analysis of the (ω, k) -space drift shows that the wave fits well to the whistler dispersion curve. The mechanism which generates the backwards propagating whistler waves is found to correspond to the normal Doppler-shifted relativistic resonance. Energy partition indicates that most of the energy in the perpendicular electromagnetic components is taken by the whistlers, while small but sufficient fraction is going into L- and R- electromagnetic modes.

Whistlers are ubiquitous very low frequency (VLF) waves, detected in the Earth radiation belts, in some cases produced in the atmosphere by lightning, studied numerically and in the space and laboratory experiments [15–17]. Electron beams injected from satellites into the ionospheric and magnetospheric plasma have resulted in emission of the whistlers mainly from the front of the beams [18]. Emission of the whistlers through normal Doppler-shifted resonance has been reported in a laboratory experiment, where the excited whistlers propagate opposite to the beam direction and their phase and group velocities are characteristic of the beam-whistler resonant cyclotron coupling [19].

The numerical model is described in Sec. II. In Sec. III the general evolution of the system and the evidence for the backwards propagating waves are presented, followed by their characterisation and identification through

altering the background magnetic field. Further, the velocity and the width of the injected beam are varied in order to prove that our Doppler relativistic resonance excitation mechanism for whistler waves is valid. Lastly, the partition of the total energy into the electromagnetic energy and sub-partition of the electromagnetic energy into whistlers and L- and R- electromagnetic modes is evaluated. Results are summarised in Sec. IV.

II. SIMULATION SETUP

Following recent works [1, 3], a 1.5-dimensional system of non-gyrotropic, super-thermal, electron beam injected into background Maxwellian plasma is employed for studying wave generation in the context of the Type-III emission, specifically to establish the (ω, k) -space drift (wave refraction) of transverse electromagnetic fields, caused by the density gradient. Fully electromagnetic relativistic particle-in-cell (PIC) code EPOCH with implemented open boundary conditions is utilised as in the study [2]. The code is developed by the collaborative computational plasma physics (CCPP) consortium of the UK researchers, funded by the Engineering and Physical Sciences Research Council (EPSRC).

The open magnetic field line between the Sun and the Earth, along which the super-thermal electron beams generating the Type-III radio bursts propagate, is represented by a constant background magnetic field B_{0x} . In the reference run the imposed value of the background magnetic field is $B_{0x} = 3.208 \cdot 10^{-4}T$, as in [2]. We allow for the x -coordinate variation of the velocity components, v_x, v_y, v_z , of all particles as well as of the electromagnetic field components, E_x, E_y, E_z, B_x, B_y and B_z , whereby the y - and z - coordinates are ignorable.

The background plasma density close to the Sun is assumed to be $n_{Sun} = 10^{14} m^{-3}$ and at the position of the Earth it drops to the $n_{Earth} = 10^6 m^{-3}$, following the parabolic profile:

$$n_e(x) = n_{Earth} + (n_{Sun} - n_{Earth}) \left(\frac{x}{L} - 1 \right)^2, \quad (1)$$

where L stands for the total size of the simulation box and x is spatial coordinate along the simulation domain. As a result of the above defined parameters, plasma beta in $x = 0$ is set to $\beta = 0.01012$.

The beam is set as a separate electron population at the left side of the domain, representing the side close to the Sun, with the density profile defined by:

$$n_{beam} = n_0 e^{-((x-L/25)/(L/40))^8}, \quad (2)$$

where $n_0 = 10^{11} m^{-3}$ is the beam density at $x = 0$. The beam density has the length of $L_{beam} = L/20$. The beam is injected at the beginning, at $t = 0$, and propagates along the density gradient in the simulation domain with a constant velocity. The beam is not replenished, *i.e.* we solve the initial value problem. Spiky density

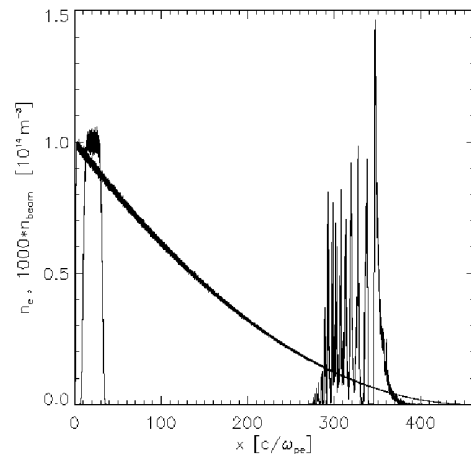


FIG. 1: Beam density multiplied by the 10^3 at the beginning (left) and at the end (right) of the reference run as a function of distance x normalised by $c/\omega_{pe}(x=0)$ depicted by two towery profiles. The parabolic shaped curve denotes the background plasma density profile.

profile of the beam at the end of the simulation, as seen in Fig. 1, is consistent with the quasi-linear theory prediction. In the reference run the average speed of the electrons in the beam is taken to be $v_{beam} = c/2$, where c is the speed of the light. The drift velocity is assumed to be equal in the perpendicular and x - directions of the simulation domain, therefore the pitch angle $\vartheta_p = 45^\circ$. The temperature of the electron beam is taken to be $T_{beam} = 6 \cdot 10^6 K$ and the temperature of the background plasma is $T_e = T_p = 3 \cdot 10^5 K$.

In the present study the three particle species, beam electrons, background electrons and background ions, are initialised each with 500 particles per cell. The size of the physical box is $L_x = 245.69m$ and the numerical box has 65000 grid points. The grid size equals to the electron Debye length found near the Sun at the location of the highest density, $\lambda_{De} = 0.00378m$.

III. RESULTS

A. Backwards propagating wave

In the reference run the choice of the background magnetic field $B_{0x} = 3.208 \cdot 10^{-4}T$ sets the ratio of the electron cyclotron and electron plasma frequency at the left side of the simulation domain to be $\omega_{ce}/\omega_{pe}(x=0) = 0.1$. The numerically studied plasma is weakly magnetised. The initialised beam traverses $\sim 3/4$ of the simulation domain in the course of the simulation, as shown in Fig. 1.

Wave activity present in the system of non-gyrotropic beam injected into the Maxwellian plasma with decreasing density profile evidenced by the perpendicular com-

ponent of the magnetic field B_z is presented in Figs. 2 (a) and (b). B_z , normalised by $e/m_e\omega_{pe}(x=0)$, is plotted as a function of the position x , normalised by $c/\omega_{pe}(x=0)$, and the time t , normalised by $1/\omega_{pe}(x=0)$. In Fig. 2 (a) the beam is seen to propagate along the x -axis with the velocity $v_{beam,\parallel} = c/(2\sqrt{2})$. In the right half of the numerical box freely escaping electromagnetic waves with slope $v = c$ are apparent after the time $\approx 500 \omega_{pe}(x=0)$, as in Refs. [1],[2].

The wave found in the left hand side of the box is created at the front edge of the beam and propagates *backwards*. Its wavelength $\lambda \approx 26.6-28.6 [c/\omega_{pe}(x=0)]$ is inferred from the contour version of the B_z time-distance plot, presented in Fig. 2 (b). Fig. 2 (c) presents the time-distance plot of perpendicular electric field component E_y , normalised by $e/cm_e\omega_{pe}(x=0)$, in which formation of the freely escaping electromagnetic wave is most clearly visible. Time-distance plots of perpendicular magnetic and electric field components exhibit the same wave activity pattern. However, backwards propagating wave is more pronounced feature in the perpendicular magnetic field, while the electromagnetic wave is more clearly seen from the perpendicular electric field.

In order to alter the properties of the generated backwards propagating wave, the background magnetic field B_{0x} is altered. Two times smaller B_{0x} yields $\omega_{ce}/\omega_{pe}(x=0) = 0.05$, while two times larger B_{0x} sets $\omega_{ce}/\omega_{pe}(x=0) = 0.2$. Time-distance plots of B_z and E_y are presented respectively in (a) and (b) panels of Figs. 3 and 4. Figs. 3 (b) and 4 (b) depict formation of the wave beats in the injection region. Fig. 3 (a) displays the case of the 2 times smaller applied B_{0x} and hence 2 times smaller ω_{ce} . The λ in this case is estimated to be $51.9-55.2 [c/\omega_{pe}(x=0)]$. Fig. 4 (a) contains the case with the B_{0x} and ω_{ce} two times larger than in the reference run. The λ is here $\approx 14.2-15.8 [c/\omega_{pe}(x=0)]$. When ω_{ce} is two times smaller than in the reference run, λ is approximately two times larger than inferred in the reference run. On the other hand, ω_{ce} two times larger yields λ approximately two times smaller than in the reference run. Backwards propagating waves are thereby confirmed to have frequency proportional to the electron-cyclotron frequency ω_{ce} , as prescribed by the dispersion relation (see Eq. 3 below for details).

1. Characterisation of the wave

Further insight into the wave activity of the system is gained through the Fast Fourier Transform (FFT) analysis. Fig. 5 displays the two-dimensional FFT of the B_z in the injection region of the reference run, with the injection region being defined as the stripe $x \in [0, 50]$ and $t \in [0, t_{end}]$. Logarithmic colour scale is employed. Additionally, in order to have better visual display, non equal steps of the colorscale are applied. The smallest step is chosen to be five times smaller than the average step and put at the largest value of the $\text{FFT}(B_z)$, be-

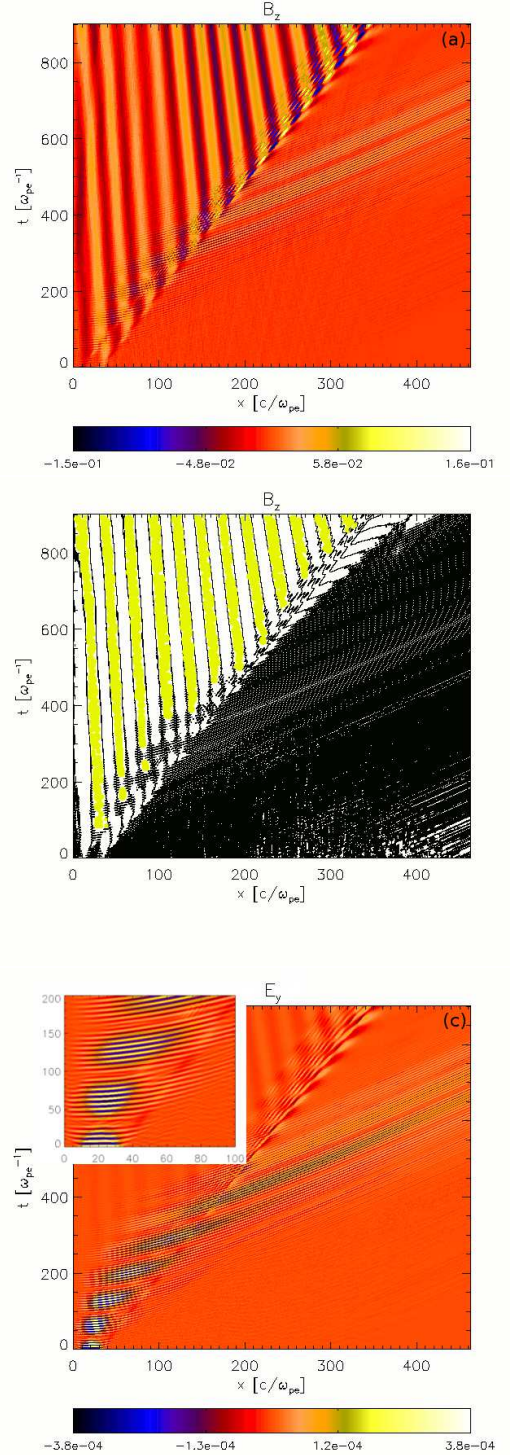


FIG. 2: (a) The magnetic field component B_z as a function of space and time in the reference run, where $\omega_{ce}/\omega_{pe}(x=0) = 0.1$. Existence of the backwards travelling wave in upper left region is evident. (b) Contour plot of the time-distance plot for B_z , used for estimating the wavelength λ of the backwards travelling wave. Beats are produced in the interaction of the $v_{beam,\perp}$ with the backwards propagating wave. (c) Time-distance plot of E_y for the same run. The insert depicts magnified part of the injection region where the beats are formed. The escaping electromagnetic radiation evolved from the formed beat of superposed $\omega_R(k_{beam})$ and $\omega_L(k_{beam})$.

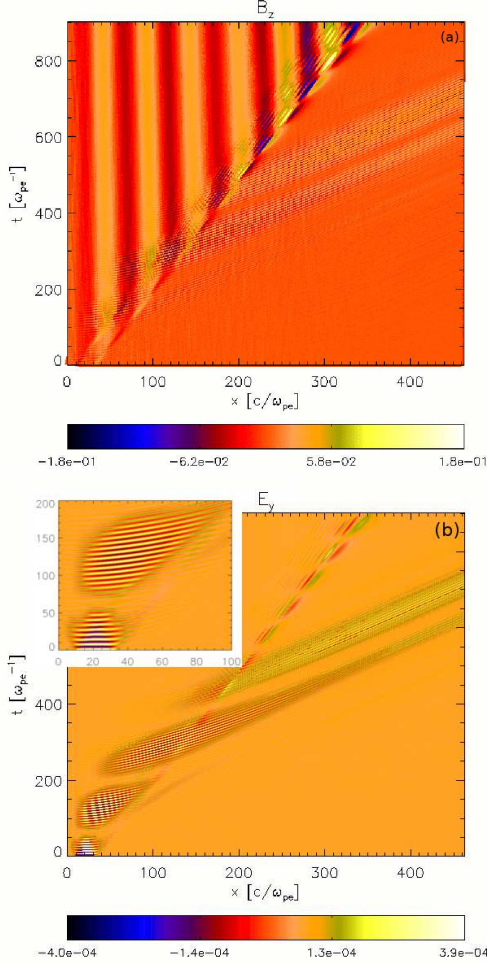


FIG. 3: (a) Time–distance plot for B_z and the $\omega_{ce}/\omega_{pe}(x=0) = 0.05$. Backwards propagating wave is seen to have ≈ 2 times larger wavelength than in the reference run. (b) Time–distance plot of E_y for the same run. The beats are formed by superposition of $\omega_L(k_{beam})$ and $\omega_R(k_{beam})$.

cause the function was seen to have significantly more variations at its larger values. The step increases uniformly for decreasing $\text{FFT}(B_z)$ and reaches its maximal value, five times larger than the average step, on the side of the minimal value of $\text{FFT}(B_z)$. In a FFT graph the group velocity is inferred as a tangent to the dispersion curves, $v_g = \partial\omega/\partial k$, and the phase velocity is a straight line passing through the origin, $v_{ph} = \omega/k$.

Fig. 5 (a) displays two initially excited high frequency wave modes. Overplotted black parabolas are 0^{th} root of the dispersion relations for the electromagnetic R-wave (higher) and L-wave (lower) with electron plasma density at the left side of the simulation box, $\omega_{pe}(x=0)$, taken. The black curve in the bottom part of the graph is 1^{st} root of the R-mode, known as the whistler wave, see *e.g.* Eqs. (3.38) and (3.41) in Ref. [20]. Whistler wave dispersion curve approaches asymptotic value $\omega_{ce}/\omega_{pe}(x=0) = 0.1$ at large k . The maxima of the $\text{FFT}(B_z)$ in the

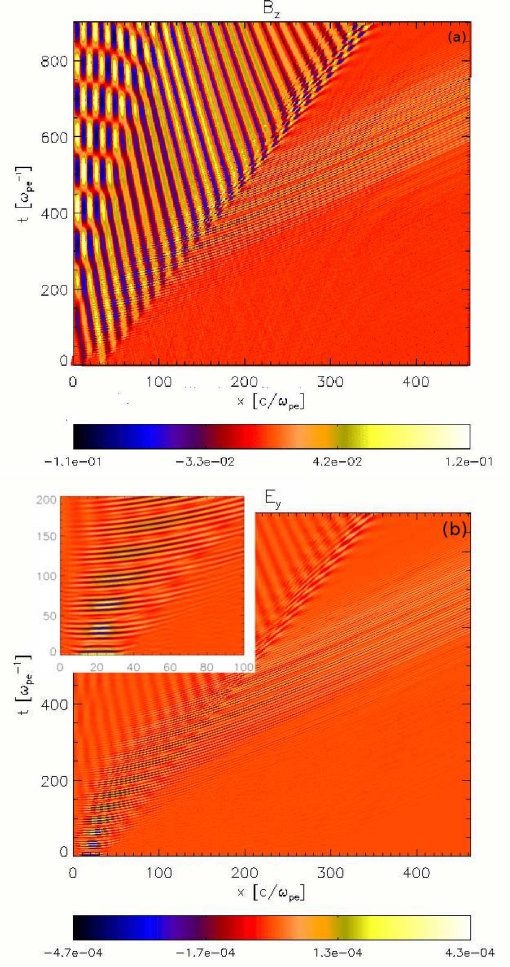


FIG. 4: (a) Time–distance plot for B_z and the $\omega_{ce}/\omega_{pe}(x=0) = 0.2$. Backwards propagating wave has wavelength ≈ 2 times smaller than the λ in the reference run. Reflection from the boundary is taking place at the left side of the domain. (b) Time–distance plot of E_y for the same run. The beats are formed by superposition of $\omega_L(k_{beam})$ and $\omega_R(k_{beam})$.

plot lie at the intersection of $k_{beam} = 2\pi/L_{beam}$ and the dispersion curves of the L and R modes. Therefore, the waves were identified as L and R waves by Schmitz and Tsiklauri [2]. The frequency difference of the two modes at $k=0$, equal to $\omega_R(k=0) - \omega_L(k=0) = \omega_{ce}/2 \cdot \{\sqrt{1 + 4\omega_{pe}^2/\omega_{ce}^2} + 1\} - \omega_{ce}/2 \cdot \{\sqrt{1 + 4\omega_{pe}^2/\omega_{ce}^2} - 1\} = \omega_{ce}$ [20], has a smaller than ω_{ce} value at $k = k_{beam}$. Superposition of the two modes with slightly different frequency results in the beating of the field oscillations, which can be seen in the upper left insert of Fig. 2 (c). The formation of the beats and the backwards propagating wave studied here takes place in the initial injection region of the beam, as seen in of Figs. 2 (a) and (b). The beats are formed by superposition of $\omega_L(k_{beam})$ and $\omega_R(k_{beam})$, *cf.* Ref. [2]. The formed wave packet starts moving from the

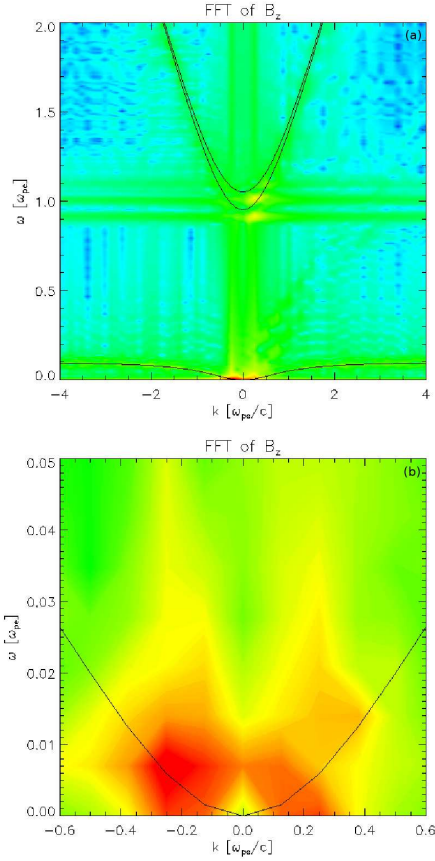


FIG. 5: (a) FFT of the B_z in the injection region of the reference run, with $\omega_{ce}/\omega_{pe}(x=0) = 0.1$, depicted in the logarithmic colour scale and non equal steps. Two modes excited with slightly different frequency around $\omega_{pe}(x=0)$ are evident in the upper part of the graph. The maxima lie at the intersection of the wavenumber prescribed by the length of the beam, $k_{beam} = 2\pi/L_{beam}$, and the 0^{th} root of the dispersion curves of the L- and R- modes. At k_{beam} the frequency difference becomes somewhat smaller than ω_{ce} . Dispersion curve of the 1^{st} root of the R- mode is seen to have asymptotic at the $\omega_{ce}/\omega_{pe}(x=0)$, in accordance with the dispersion relation for the L-waves, $k = \omega/c \cdot \{1 + \omega_{pe}^2/(\omega(\omega_{ce} - \omega))\}^{1/2}$ in Ref.[20]. (b) Enlarged lower part of the FFT graph from the top panel, depicting the area around whistler curve in which the backwards travelling ω_{ce} harmonics exhibit strongly enhanced B_z .

injection region into the the lower density region. The almost horizontal lines of the E_y visible in the insert in the time-distance plot become inclined (Fig. 2 (c)) due to the wave refraction caused by the density gradient, thereby indicating decrease of the phase velocity, v_{ph} , to finite values. The decrease of the phase velocity inferred in Figs. 2 (a) and (c) (see also Fig. 5 from Ref. [2] for its dynamic in time version) continues throughout the region of the decreasing density. At the time $\approx 500 \omega_{pe}(x=0)$ it becomes almost equal to the speed of light, $v_{ph} = c$. The wave packet has eventually turned into a freely es-

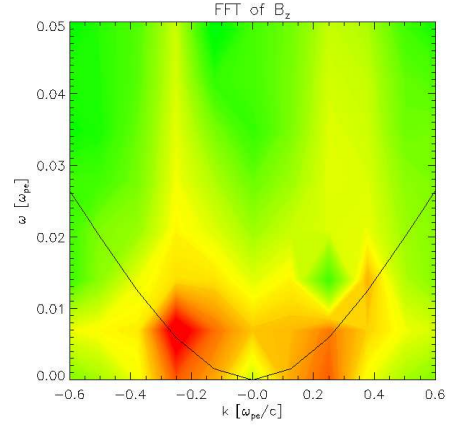


FIG. 6: FFT of B_z in the whistler wave enhanced area in the case when the two times narrower beam than in the reference run was imposed. Overplotted black curve depicts the whistler wave dispersion relation.

caping electromagnetic wave, as reported by Ref. [2], due to (ω, k) -space drift, *i.e.* wave refraction.

Fig. 5 (b) presents enlarged lower part of the FFT graph from the top panel. Whistler dispersion relation curve is overplotted with black curve. Enhanced magnetic field component B_z evident along the whole whistler curve is seen to be strongly enhanced at small ω and a small k .

Fig. 6 presents zoom into whistler region of the FFT of B_y for the case when the beam is taken to have half of the width of the reference run. Comparison with Fig. 2 (c) leads to a conclusion that the change of the width of the beam does not play a role for whistlers.

FFT graphs zoomed into the whistler area for the B_{0x} taken to be 2 times smaller and 2 times larger than in the reference run are presented at Figs. 7 (a) and (b), respectively. In all the examined cases (applied ω_{ce} , $1/2 \cdot \omega_{ce}$ and $2 \cdot \omega_{ce}$) the initially excited backward propagating harmonics exhibit enhancements of the B_z along the whistler dispersion curves and are therefore conclusively identified as whistlers.

B. Excitation of the whistler waves

In order to determine how the backwards propagating whistlers are generated, the following dispersion relation for whistlers is employed [21]:

$$\omega = \omega_{ce} \frac{k^2 c^2 |\cos(\vartheta)|}{\omega_{pe}^2 + k^2 c^2}, \quad (3)$$

where θ stands for the angle between \vec{k} and \vec{B} . Further, relativistic Doppler-shifted cyclotron resonance condition is applied:

$$\frac{s}{\gamma} \omega_{ce} = \omega - \vec{k}_{\parallel} \cdot \vec{v}_{beam, \parallel}, \quad (4)$$

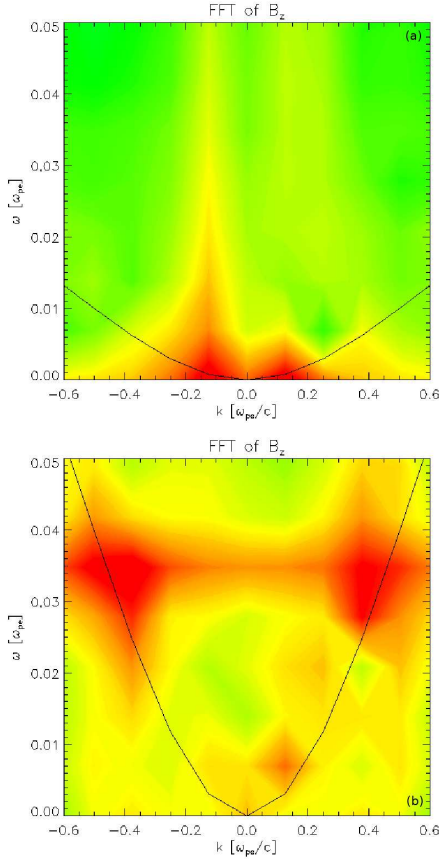


FIG. 7: (a) FFT graph for B_z at prescribed $\omega_{ce}/\omega_{pe}(x=0) = 0.05$. Backwards travelling harmonics have the strong enhancement of the B_z at smaller angular frequencies ω and smaller wavenumbers k than in the reference run. (b) FFT graph for B_z at prescribed $\omega_{ce}/\omega_{pe}(x=0) = 0.2$. Backwards travelling harmonics have enhancement of the B_z at larger wavenumbers k and larger angular frequency ω than in the reference run.

where s represents particular cyclotron harmonic and γ is the Lorentz factor, $\gamma = (1 - v_{beam,\parallel}^2/c^2)^{-1/2} \approx 1.069$. The resonant beam electrons drift in the opposite direction as the whistlers, thereby yielding the term $\vec{k}_{\parallel} \cdot \vec{v}_{beam,\parallel}$ to be negative. Whistler mode waves exist in the range $0 < \omega < \omega_{ce}$. Therefore, right hand side of Eq.(4) is positive and, consequently, the wave harmonic number s is positive, $s > 0$. Relativistic correction accounted for in Eq.(4) is found to play a decisive role in establishing the point of resonance between the electrons and the whistler waves, analogously to Ref. [22]. Combination of Eqs. (3) and (4) yields the equation for the velocity of the relativistic beam electrons in the Doppler-shifted resonance with the whistler waves:

$$|v_{beam,\parallel}| = \frac{c}{\omega_{pe}} \left| \frac{s}{\gamma} \omega_{ce} - \omega \right| \sqrt{\frac{\omega_{ce} |\cos(\vartheta)| - \omega}{\omega}}, \quad (5)$$

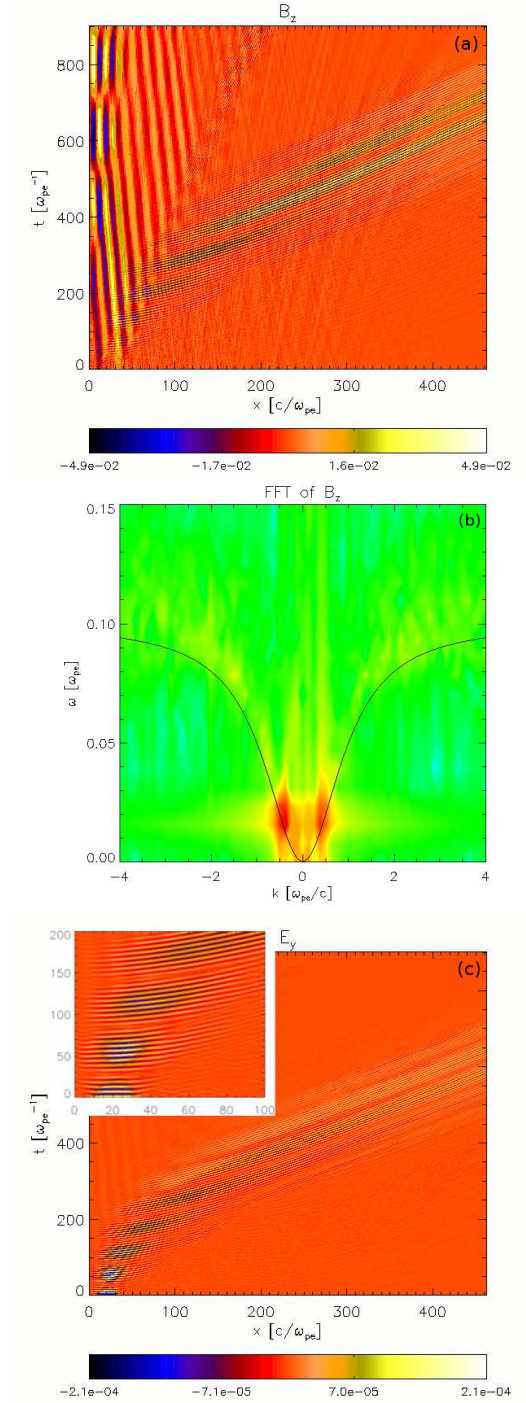


FIG. 8: (a) Time-distance plot of B_z for the case when the beam is two times slower than in the reference run. The backwards propagating harmonics are evident in the wake-side of the beam. (b) FFT of the B_z enlarged in the whistler area. The enhancement of the B_z along the whistler dispersion curve is evident. The strong enhancement of B_z takes place at larger k and ω than in the reference run. (c) Time-distance plot of E_y for the same run.

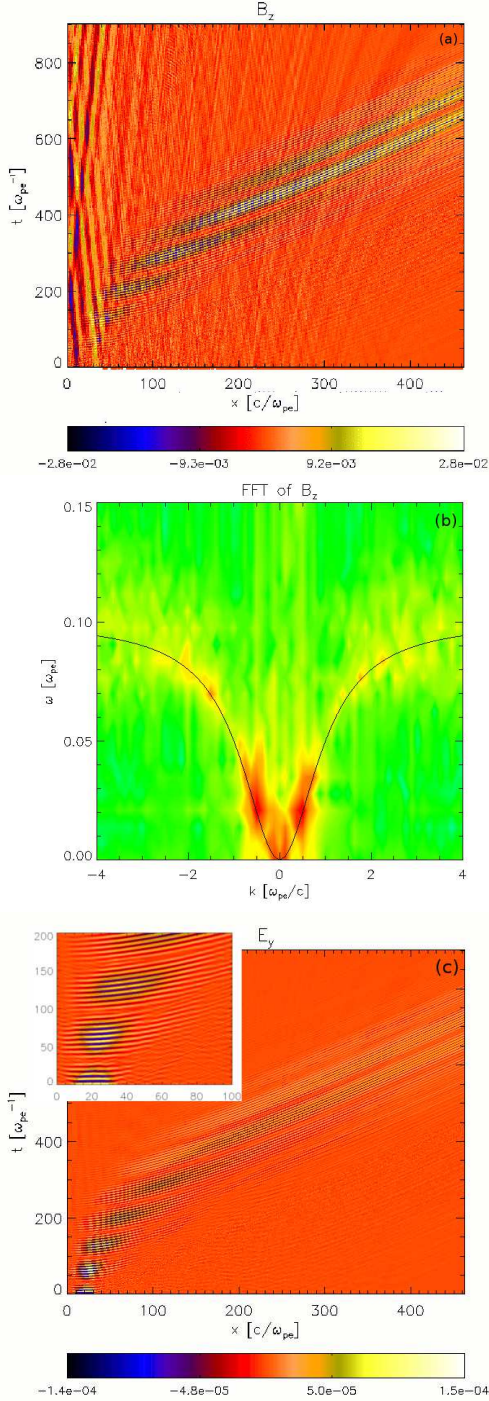


FIG. 9: (a) Time–distance plot of B_z for the case when the beam is three times slower than in the reference run. A clear pattern of backwards propagating harmonics is evident only in the injection region. (b) FFT of the B_z enlarged in the whistler area. The enhancement of the B_z is more spread to larger wavenumbers. The strongest enhancement takes place also at k and ω bigger than in the reference run. (c) Time–distance plot of E_y for the same run.

which is rewritten as a cubic equation in ω :

$$\begin{aligned} \omega^3 - \omega^2 \cdot \omega_{ce} (|\cos(\vartheta)| + 2\frac{s}{\gamma}) \\ + \omega [v_{\parallel}^2 \frac{\omega_{pe}^2}{c^2} + \frac{s}{\gamma} \omega_{ce}^2 (2|\cos(\vartheta)| + \frac{s}{\gamma})] \\ - \frac{s^2}{\gamma^2} \omega_{ce}^3 |\cos(\vartheta)| = 0. \end{aligned} \quad (6)$$

The imposed initial condition specifies the ratio $\omega_{ce}/\omega_{pe}(x=0)$, where whistler dispersion curve has the asymptotic, $\omega/\omega_{pe}(x=0) = \omega_{ce}/\omega_{ce}(x=0)$, as seen *e.g.* in Fig. 5 (a). Higher order cyclotron resonances, $s > 1$, are found to yield solutions above the asymptotic. The only acceptable solution is found to be at the $s = 1$, which is normal Doppler-shifted relativistic resonance. Resonance patterns apparent in the FFT graphs, closely related to the harmonics $s = 1$, are presented below.

In the reference run the prescribed ratio is $\omega_{ce}/\omega_{pe}(x = 0) = 0.1$. The root of Eq.(6) yields $\omega_0(s = 1)/\omega_{pe}(x = 0) = 0.0058$. This finding is closely resembling the resonance apparent in the FFT graph of the B_z component at $k \approx 0.25$ presented in Fig. 5 (b), that clearly sits on the whistler dispersion curve.

When $\omega_{ce}/\omega_{pe}(x = 0) = 0.05$ the solution of Eq.(6) gives $\omega_0(s = 1)/\omega_{pe}(x = 0) = 0.00083$. This corresponds well with resonance at the $k \approx 0.09$ seen on Fig. 7 (a). In this particular case the smallest normalised angular frequency that can be resolved is $\omega_{min}/\omega_{pe}(x = 0) = 0.0011$, which is larger than the value we calculated. The choice of the stripe boundaries in the time–distance plot determines the minimal normalised wavenumber to be $k_{min} = 0.1257$, which is larger from the wavenumber determined from the whistler dispersion relation. Therefore, in this case it is not possible to see the exact value of the calculated resonance value in the FFT graph.

In the case $\omega_{ce}/\omega_{pe}(x = 0) = 0.2$ the solution of Eq.(6) yields $\omega_0(s = 1)/\omega_{pe}(x = 0) = 0.0314$. The solution corresponds reasonably well with resonant enhancements in the FFT graph apparent at $k \approx 0.42$, as depicted in Fig. 7 (b), which, again, closely follow whistler dispersion relation.

In order to support the normal relativistic Doppler-shifted relativistic resonance as the mechanism which excites whistlers in the wake–side of the beam, velocity of the beam is altered to $c/4$ and $c/6$, as presented in Figs. 8 and 9, respectively. Figs. 8 (a) and 9 (a) display the time–distance graph for the magnetic field component B_z for the v_{beam} equal to $c/4$ and $c/6$, respectively. On the wake side of the beam propagating with $v_{beam} = c/4$ the backwards propagating waves are apparent. In the case of the $v_{beam} = c/6$ they are pronounced only in the injection region.

Figs. 8 (b) and 9 (b) display the FFT of the magnetic field component B_z for the case of the v_{beam} equal to $c/4$ and $c/2$, respectively. The enhanced B_z is seen to be more pronounced along the whistler curve also at the larger wavenumbers k . For the case of the beam velocity

$v_{beam} = c/4$ the solution of Eq.(6) is $\omega_0(s=1)/\omega_{pe}(x=0) = 0.0173$. This is reasonably well confirmed in Fig. 8 (b) at $k \approx 0.44$ in the resonant area. In the case of the $v_{beam} = c/6$ the $\omega_0(s=1)/\omega_{pe}(x=0) = 0.0272$. This corresponds well with the resonant areas in the FFT of B_z graph presented in Fig. 9 (b) at $k \approx 0.57$. In the case of the slower beam there is also more intensity of the magnetic field component B_z spread along the whistler curve, *i.e.* also at larger frequencies and wavenumbers.

The width of the beam does not enter Eq.(6) and, as evidenced in Fig. 6, does not influence the excitation of the whistlers. On the other hand, change of the beam velocity enters Eq.(6) as $v_{beam,\parallel} = v_{beam}/\sqrt{2}$ and the yielded solutions, which are the Doppler-shifted relativistic resonance solutions, are found to correspond well to the inferred strong field enhancements.

The backward propagating whistler mode waves are found to be excited in the injection region already at the initial time. The whole electron beam is placed in the simulation box at the beginning. As the beam does not cross any boundary, no transition radiation is observed, as in Ref. [23]. The beam has approximately three orders of magnitude smaller particle number density than the ambient plasma in the injection region, $x \in [0, 50]$ [$c/\omega_{pe}(x=0)$], as seen in Fig. 1. Such a beam is not dense enough to form a virtual cathode, as in Ref. [24], which would result in the beam modulation such as observed in Ref. [25]. The beam in the simulation has very small density fluctuations at the initial time, which grow during the simulation and, due to quasilinear relaxation, develop into the spiky density profile at the end, as seen in Fig. 1. Slight beam particle density variation in the beam particle temporal profile, less than 10%, is apparent only when the beam reaches $x = 57$ [$c/\omega_{pe}(x=0)$] and from that time on the variation of the beam particle density is seen to increase. However, whistlers are evident already in the injection region, $x \in [0, 50]$ [$c/\omega_{pe}(x=0)$], where there is no sign of the beam density variation. Compressibility of the whistler mode can yield the whistlers additionally perturbing the beam density. Thus we conclude that the whistler mode waves are occurring due to the normal Doppler-shifted resonance with the drifting relativistic beam electrons.

C. Partition of the energy

Analysis of the electromagnetic energy of the system is performed starting from the Poynting's theorem for electromagnetic energy as a function of time:

$$w(t) = \int \left[\frac{1}{2} \varepsilon_0 \vec{E}(x, t)^2 + \frac{1}{2\mu_0} \vec{B}(x, t)^2 \right] dx, \quad (7)$$

where ε_0 stands for the electric permittivity of the vacuum, μ_0 for the magnetic permeability of the vacuum and \vec{E} and \vec{B} are the electric and the magnetic field, respectively. The electric and magnetic field can be decomposed

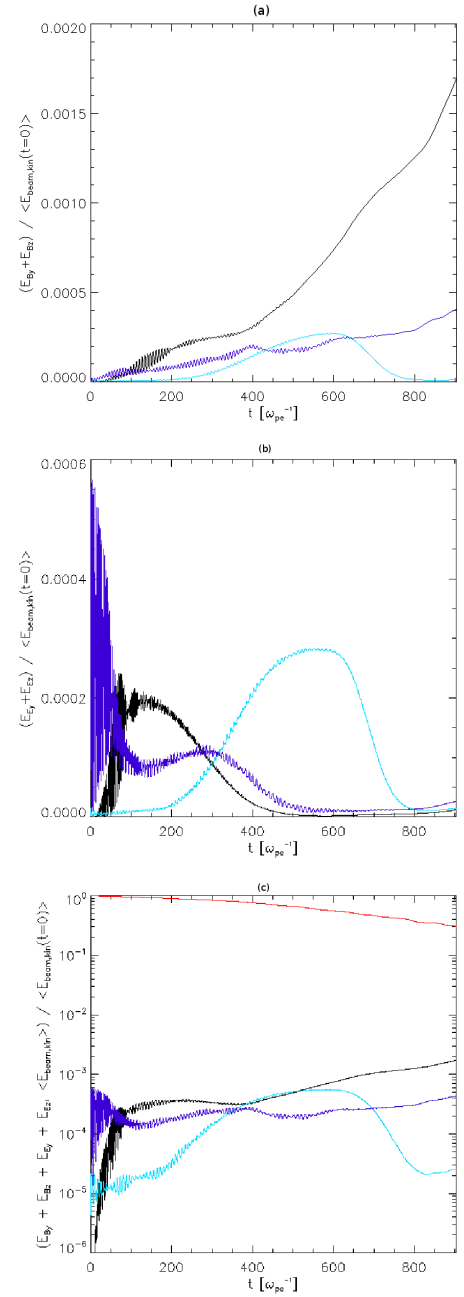


FIG. 10: (a) Energy partition in the perpendicular components of the magnetic field, B_y and B_z , normalised with the initial kinetic energy of the beam as a function of time. (b) Energy partition in the perpendicular components of the electric field, E_y and E_z , normalised with the initial kinetic energy of the beam as a function of time. (c) Partitioned total electromagnetic energy of the perpendicular components, B_y , B_z , E_y , E_z , and the beam kinetic energy (uppermost, decreasing, curve) normalised with the initial kinetic energy of the beam as a function of time. At its peak the perpendicular electromagnetic energy of the generated electromagnetic radiation is seen to be $\approx 0.054\%$ of the initial beam kinetic energy.

into the Cartesian components:

$$\begin{aligned}\vec{E}(x, t) &= \vec{E}_x(x, t) + \vec{E}_y(x, t) + \vec{E}_z(x, t) \\ \vec{B}(x, t) &= \vec{B}_x(x, t) + \vec{B}_y(x, t) + \vec{B}_z(x, t)\end{aligned}\quad (8)$$

The x component of the electric field is contributing to the electrostatic energy, while the x component of the magnetic field after subtraction of the prescribed B_{0x} is in the order of numerical noise in our numerical simulations. The perpendicular components, y and z , of the electric and magnetic fields are contributing both to the whistler and electromagnetic wave energies.

At every given instant of time the position of the beam is calculated and the time–distance plot is divided into three parts: A part occupied by the whistlers, from left boundary of the numerical box to the back edge of the beam, a part occupied by the beam, stretching between the front and the back edges of the beam, and a part in which the freely escaping electromagnetic radiation is found, from front edge of the beam till the right boundary of the box. The initial beam kinetic energy is calculated following Ref. [3] and found to be $\langle E_{beam,kin}(t=0) \rangle = 9.94607 \cdot 10^{-3} J$. Calculated perpendicular electromagnetic energy components for the reference run are divided by the initial kinetic energy of the beam and presented in Fig. 10. Whistlers are seen to originate at the front edge of the beam, however the beats (created by the superposition of L– and R– electromagnetic waves) leading to the freely escaping electromagnetic radiation are taking place in the region of the beam or even slightly behind it. Thereby, the perpendicular electromagnetic energy contained in the beam is presented separately. Black curve depicts the energy in whistlers, cyan is for the energy of the electromagnetic radiation and blue curve depicts the fraction of the perpendicular magnetic energy in the beam (color online). Fig. 10 (a) presents the perpendicular magnetic field energy as a function of time. The fraction of the energy taken by the whistlers is seen to be largest and increasing with time. The part of the perpendicular magnetic energy contained in the beam is smaller and slightly increasing with the time. Electromagnetic waves are found to contain very little of the perpendicular magnetic energy initially. Their energy is seen to grow up to a limit, and then to decrease due to the distribution becoming a ring as established in Fig. 4 of Ref. [2]. Fig. 10 (b) presents the partitioned perpendicular electric field energies as a function of time. In the perpendicular electric field energy the whistlers are seen to take less of the energy than the electromagnetic part. However, the whistlers contain substantially more energy in the perpendicular magnetic than in the perpendicular electric field, approximately 70 times more by the end of the simulation. Therefore, the total perpendicular electromagnetic energy budget, as presented in Fig. 10 (c), shows that the largest fraction of the energy is taken by the whistler waves. The whistlers, taking $\approx 58\%$ of the perpendicular electromagnetic energy, are consuming only 0.096% of the initial beam kinetic energy. Decrease of the beam kinetic en-

ergy divided by the initial beam kinetic energy in time is presented with the uppermost, red, curve (color online). Escaping L– and R– electromagnetic wave energy peaks at 0.1% of the beam initial energy. This is comparable to the other mechanisms for the Type–III radio burst generation.

IV. DISCUSSION AND SUMMARY OF THE RESULTS

1.5–dimensional system of the magnetised background Maxwellian plasma and the injected low density relativistic beam of electrons is numerically studied by utilising PIC code EPOCH. Background magnetic field is constant in each run and it mimics a magnetic field line from the Sun to the Earth. Background plasma density falls from the $n_{Sun} = 10^{14} m^{-3}$, on the left hand side of the box, to the $n_{Earth} = 10^{-6} m^{-6}$ on the right hand side of the box. Following Ref.[1], the non-gyrotropic beam injected in such a system is found to release the freely escaping electromagnetic radiation. Ref.[2] established the electromagnetic radiation being generated due to the (ω, k) –space drift (*i.e.* wave refraction), when the non-gyrotropic beam propagates along the decreasing density profile. In this study a new feature, the wave component travelling backwards, is found in the perpendicular components of the electromagnetic field. In order to complete the picture of the non-gyrotropic beam of the Type–III emission mechanism, the features, characterisation and the exciting mechanism of the backwards propagating waves are presented in this study.

Constant background magnetic field was varied in different runs, thereby changing the electron–cyclotron frequency. As a consequence, the frequency of the wave propagating backwards from the front of the beam is found to be proportional to the electron–cyclotron frequency. Fast Fourier Transform analysis of the (ω, k) –space is performed and the backwards travelling harmonics are identified as the whistler mode waves. In order to infer possible mechanism for the wave generation, combination of the Doppler-shifted relativistic resonance condition and the whistler dispersion equation is solved. The wave is found to be generated by the normal Doppler-shifted relativistic resonance. Width of the beam has been varied and, as expected from Eq.(6), resonant excitation of whistlers was not affected. However, when the beam velocity is varied, the change of the resonance is apparent, in accordance with the solutions of Eq.(6). Large fraction, $\approx 58\%$, of the energy of the perpendicular electromagnetic field components goes into whistlers. In turn, the latter constitute 0.096% of the electron beam initial energy. The perpendicular electromagnetic energy of the generated electromagnetic radiation at its peak amounts to $\approx 0.054\%$ of the initial beam kinetic energy.

A wave component travelling backwards in the numerical system in which non-gyrotropic beam excites electromagnetic radiation resembling the Type–III emission

is conclusively identified as the whistler mode wave. It is shown to be excited by the normal Doppler-shifted relativistic resonance. Whistlers propagating backwards while Type-III propagates ahead of the electron beam is a possible observable for the in-situ measurements by the spacecrafts in the solar wind. Simultaneous detection of the related whistlers and the Type-III burst could be an observational confirmation of the non-gyrotropic beam mechanism of exciting the Type-III emission taking place. To our knowledge only associated Langmuir waves have been detected in-situ [6].

Acknowledgements The EPOCH code used in this research was developed under UK Engineering and Physics Sciences Research Council grants

EP/G054940/1, EP/G055165/1 and EP/G056803/1. The simulations were run on the HPC clusters Andromeda of the Astronomy Unit, Queen Mary University of London, and Minerva of the STFC-funded UKMHD consortium at the University of St. Andrews and the University of Warwick. M.S. is funded by the Leverhulme Trust Research Project Grant RPG-311. D.T. is financially supported by STFC consolidated Grant ST/J001546/1, the Leverhulme Trust Research Project Grant RPG-311 and HEFCE-funded South East Physics Network (SEPNET). Authors would like to thank the anonymous referee whose suggestions helped in improving the article.

-
- [1] D. Tsiklauri, Phys. Plasmas **18**, 052903 (2011).
 - [2] H. Schmitz, D. Tsiklauri, Phys. Plasmas **20**, 062903 (2013).
 - [3] R. Pechhacker, D. Tsiklauri, Phys. Plasmas **19**, 112903 (2012).
 - [4] A. Krüger, Introduction to solar radio astronomy and radio physics, D. Reidel Publishing Company (1979), pp. 81-103.
 - [5] G. A. Dulk, J. L. Steinberg, S. Hoang, Astron. Astrophys. **141**, 30-38 (1984).
 - [6] R. P. Lin, D. W. Potter, D. A. Gurnett, and F. L. Scarf, Astrophys. J. **251**, 364 (1981).
 - [7] M. J. Aschwanden, *Particle acceleration and kinematics in solar flares* Sp. Sci. Rev. **101**, 1-227 (2002).
 - [8] D. Melrose, *Plasma emission - A review* Sol. Phys. **111**, 89-101 (1987).
 - [9] A. Nindos, H. Aurass, K. L. Klein, G. Trottet, Sol. Phys. **253**, (2008).
 - [10] M. Pick, N. Vilmer, Astron. Astrophys. Rev. **16**, 1-153 (2008).
 - [11] V. L. Ginzburg and V. V. Zhelezniakov, Sov. Astron. **35**, 694 (1958).
 - [12] P. A. Robinson, Solar Phys. **139**, 147 (1992).
 - [13] I. H. Cairns and A. J. Willes, Phys. Plasmas **12**, 052315 (2005).
 - [14] D. M. Malaspina, I. H. Cairns, and R. E. Ergun, J. Geophys. Res. **115**, A01101 (2010).
 - [15] R. H. Holzworth, M. P. McCarthy, R. F. Jacobson, A. R. Willcockson, and D. E. Rowland, J. Geophys. Res. **116**, A06306 (2011).
 - [16] C. Krafft, A. Volokitin, Phys. Plasmas **5**, 4243-4252 (1998).
 - [17] A. Volokitin, C. Krafft, G. Matthieussent, Phys. Plasmas **4**, 4126-4135 (1997).
 - [18] M. Starodubtsev, C. Krafft, B. Lundin, P. Thévenet, Phys. Plasmas **6**, 2862-2869 (1999).
 - [19] M. Starodubtsev, C. Krafft, Phys. Rev. Lett. **83**, 1335-1338 (1999).
 - [20] R. O. Dendy, Plasma Dynamics, Clarendon Press Oxford (1990), pp. 41-43.
 - [21] A. V. Stepanov, V. V. Zaitsev, V. M. Nakariakov, Coronal Seismology, WILEY-VCH (2012), pp. 118-125.
 - [22] C. S. Wu, L. C. Lee, Astron. Astrophys. **230**, 621-626 (1979).
 - [23] M. Starodubtsev, C. Krafft, B. Thévenet, P. Kostrov, Phys. Plasmas **6**, 1427-1434 (1999).
 - [24] P. L. Pritchett, R. M. Winglee, J. Geophys. Res. **92** (1987).
 - [25] M. Starodubtsev, C. Krafft, B. Thévenet, IEEE Trans. Plas. Sci. **28**, 367-370 (2000).